Influence of Annealing and Composition on Crystal Structure of Mixed-Halide, Ruddlesden-Popper Perovskites.

Niara E. Wright a,b,*, Xixi Qin a,c, Junwei Xu d, Leah L. Kelly d, Steven P. Harvey e, Michael F. Toney d,f, Volker Blum a,c,g, Adrienne D. Stiff-Roberts a,b,*.

- ^a University Program in Materials Science and Engineering, Duke University, Durham, NC, 27708, USA
- ^b Department of Electrical and Computer Engineering, Duke University, Durham, NC, 27708, USA
- ^c Thomas Lord Department of Mechanical Engineering and Materials Science, Duke University, Durham, NC, 27708, USA
- d Stanford Synchrotron Radiation Lightsource, SLAC National Accelerator Laboratory, Menlo Park, CA, 94025, USA
- e National Renewable Energy Laboratory, Golden, CO, 80401, USA
- ^f Department of Chemical and Biological Engineering, University of Colorado Boulder, Boulder, CO, 80309, USA
- g Department of Chemistry, Duke University, Durham, NC, 27708, USA

ABSTRACT: Mixed-halide two-dimensional (2D) hybrid organic-inorganic perovskites (HOIPs) offer an important opportunity to control the bandgap for applications in optoelectronic devices. This study focuses on phenethylammonium lead halide [(PEA)₂Pb(I_{1-x}Br_x)₄] films, the pure iodide form of which is one of the most widely studied optically active 2D perovskite systems. Resonant infrared, matrix-assisted pulsed laser evaporation (RIR-MAPLE) is used to grow films to explore the effects of post-growth annealing and mixed-halide composition. Composition, crystal structure, and optical properties are studied for as-grown and annealed films of (PEA)₂Pb(I_{1-x}Br_x)₄ for x = 0, 0.25, 0.5, 0.75, and 1. First-principles calculations are used in conjunction with the experimental data to explain mixed-halide behavior that does not trend monotonically with bromide content. Important results of this work are: (i) X-ray diffraction (XRD) reveals evidence for halide phase separation around x = 0.25, consistent with first-principles calculations, whereas no phase separation is observed for x = 0.5 and above; and (ii) a unique photoluminescence (PL) peak splitting is observed for x = 0.75, a composition for which no compositional phase separation is observed. The PL splitting is tentatively explained by the coexistence of two distinct types of halide short-range ordering at x = 0.75. Overall, this study demonstrates that mixed-halide n = 1 Ruddlesden-Popper perovskites are not simple random alloys, but that instead, they display distinct site and ordering preferences of the different halide anions. These preferences are critical to understand and rationally tune the properties of the materials.

INTRODUCTION

Hybrid organic-inorganic perovskites (HOIPs) have been explored as absorbers and emitters in photovoltaic devices¹⁻⁸ and light emitting diodes (LEDs)⁹⁻¹³, respectively, due to their high electron mobility, strong photoluminescence, high absorption coefficient, and tunable bandgap.14-18 Three-dimensional (3D) hybrid perovskites are semiconductors with the structure ABX3, where A is an organic cation, B is a metal cation (e.g. Pb2+ or Sn2+) and X is a halide anion (I-, Br-, Cl-). 3D perovskites have been employed with great success as absorbing materials in photovoltaic devices.^{3,8,19-21} For example, 3D HOIPs have been used higher bandgap material perovskite/silicon²² and perovskite/CIGS (copper indium gallium selenium)²³ tandem solar cells to produce research devices that have reached power conversion efficiencies (PCEs) of 29.1% and 24.2%, respectively.24 In 3D HOIPs, halide alloying is critical for finely tuning the bandgap to create the higher bandgap absorber necessary in tandem solar cells.^{19,25} One challenge of harnessing the tunable bandgap in mixed-halide 3D HOIPs is halide migration, including phase segregation to form domains of I-rich and Br-rich phases.^{25–29} Ion migration may also contribute to hysteresis that reduces PCE in perovskite solar cells.^{30,31}

So-called quasi-two-dimensional (quasi-2D) HOIPs^{1,17} provide an alternative approach to tune the bandgap, 32,33 with an additional hope of circumventing the challenge of halide migration in 3D HOIPs. Quasi-2D HOIPs have an R₂A_{n-} $_{1}B_{n}X_{3n+1}$ structure in which R is a larger organic cation (compared to the A organic cation) and *n* is the number of B-X octahedra layers (n > 1). The bandgap of quasi-2D perovskites can already be tuned by changing the n number of B-X octahedra layers, without introducing mixed-halide alloys. In addition, the quasi-2D HOIPs can help address the well-known stability challenges in 3D perovskites ($n \rightarrow$ ∞) because the larger organic cation (R) acts as a hydrophobic layer that protects the 3D-like HOIP sublayers from humidity.^{4,34} However, creating quasi-2D HOIP thin films with only a single, precisely defined n value across an entire film has been difficult to demonstrate consistently for large *n*, somewhat limiting the bandgap tunability achievable with this particular method. 17,35,36

Pure 2D HOIPs (n = 1) have been incorporated into photovoltaic device structures as wider bandgap, passivating layers on top of 3D HOIP absorbers to improve the overall long-term device stability.^{3,37} One possible configuration for two-dimensional (2D) hybrid perovskites is the R2BX4 structure in which R is a larger, singly charged organic cation, such as phenethylammonium (PEA = $C_8H_{12}N^+$) or butylammonium (BA = $C_4H_{12}N^+$). Introducing these larger organic cations reduces the dimensionality of the inorganic component in one direction by physically separating the metal halide octahedra into sheets. 14,15,38,39 The alternating organic cation bilayers and metal halide octahedra can be viewed as the thinnest variant of halide perovskite quantum wells, giving 2D HOIPs a larger bandgap than their quasi-2D and 3D counterparts because of quantum confinement effects. Importantly, the bandgap of 2D HOIPs can be tuned by using halide alloying, for example as a means to yield different emission wavelengths in LEDs. 12,13,17 Despite these advantages for bandgap tunability, especially applied to LEDs, the thin-film deposition of mixed-halide 2D HOIPs faces some challenges. Traditional, solutionbased deposition techniques generally require postgrowth annealing or hot casting to form the 2D HOIP crystal structure.36,40-42 In the context of tandem active regions or passivating layers for solar cells, the required annealing could degrade interfaces or underlying material layers. Alternatively, La Placa et al. used traditional thermal evaporation to produce mixed-halide 2D HOIP films without requiring annealing. However, contamination of the evaporation chamber by residual precursor material from previous growths prevented deposition of the intended film compositions.43

This work focuses on a different thin film deposition technique for 2D HOIPs, namely, resonant infrared, matrix-assisted pulsed laser evaporation (RIR-MAPLE). 44,45 RIR-

MAPLE is a modified pulsed laser deposition technique that uses a low energy Er:YAG laser (peak wavelength at 2.94 µm) to sublimate the matrix solvent in a frozen target solution of hybrid perovskite precursors (Figure 1a). Because the laser energy is resonant only with the vibrational modes of O-H bonds present in the matrix solvent (monoethylene glycol, MEG), the resulting sublimation transfers kinetic energy to precursor materials within the target solution such that the precursors are ejected from the target and gently transferred to the substrate (Figure 1b). It is important to note that, while deposition occurs under an active vacuum (approx. 2×10-5 Torr), a small amount of the primary solvent (dimethyl sulfoxide, DMSO) arrives at the substrate, due to entanglement with precursor materials in liquid phase in the immediate vicinity of the target area irradiated by the laser. In contrast, most of the matrix solvent in vapor phase is removed from the chamber by the pumping required to maintain vacuum. RIR-MAPLE has already demonstrated high-quality thin film deposition of 2D and 3D HOIPs.21,46-49

In this study, the roles of annealing and mixed halide composition in determining the crystal structure of 2D, PEA-based, mixed halide HOIPs (n=1) deposited by RIR-MAPLE are articulated. While the PEA-based, quasi-2D HOIP system has been investigated extensively, $^{1,9,36,50-53}$ less is known about the behavior of mixed-halide compositions in the pure 2D system. 41,43,54 RIR-MAPLE target solutions with precursor materials [phenethylammonium iodide ((PEA)I), phenethylammonium bromide ((PEA)Br), lead iodide (PbI₂), and lead bromide (PbBr₂)] in dimethyl sulfoxide (DMSO, primary solvent) and MEG (matrix solvent) were used to create mixed halide 2D HOIP films: (PEA)₂Pb($I_{1-x}Br_x$)₄ for x = 0, 0.25, 0.5, 0.75, and 1.

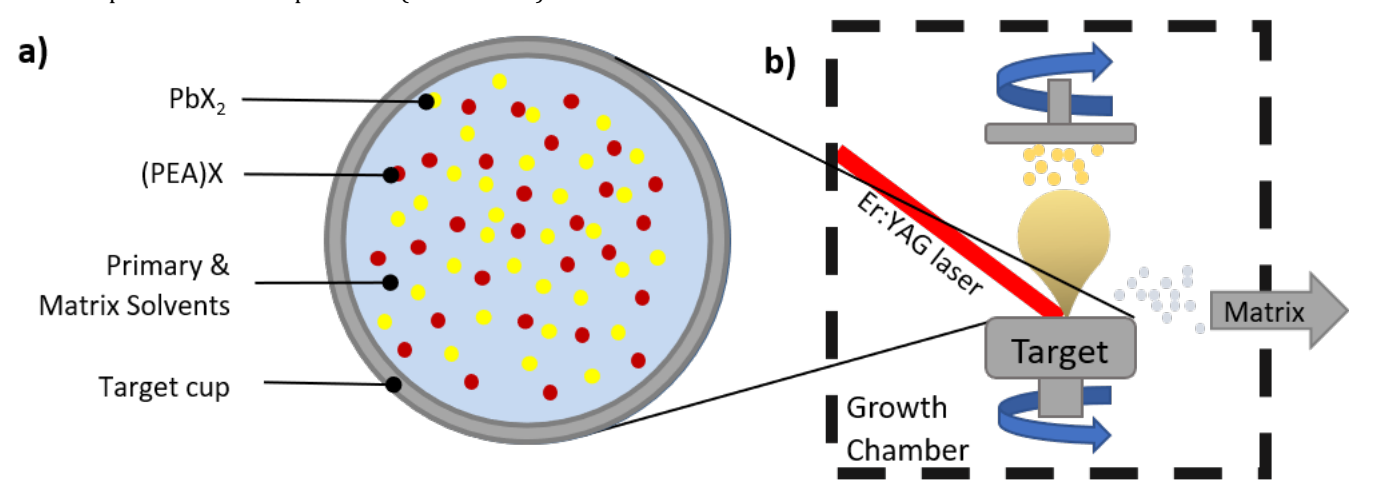


Figure 1. RIR-MAPLE. (a) Schematic diagram of the frozen target solution that consists of a primary solvent (DMSO), a matrix solvent (MEG), and precursor materials PbX_2 (yellow) and (PEA)X (red). **(b)** Schematic diagram of the RIR-MAPLE growth chamber used to deposit perovskite thin films.

The values of x correspond to the fraction of bromide added to the target solution. The amount of bromide that is incorporated into the deposited film could deviate slightly from the composition of the target. However, the absence of excess PbX2 or PEAX in the resulting films shows that the deviation between input and incorporated compositions must be limited (if any) and is not expected to significantly impact the results of this study. The impact of postgrowth annealing was determined by comparing as-grown and annealed mixed-halide (PEA)₂Pb(I_{1-x}Br_x)₄ thin films by characterization techniques including time-of-flight secondary ion mass spectrometry (TOF-SIMS) for compositional analysis throughout the depth of the film, grazingincidence wide angle x-ray scattering (GIWAXS) and X-ray diffraction (XRD) for perovskite crystal structure, UV-vis absorbance (UV-vis) and photoluminescence (PL) spectroscopy for optical behavior, as well as energy dispersive spectroscopy (EDS) to compare halide distribution across the film surface, and scanning electron microscopy (SEM) and atomic force microscopy (AFM) to compare film morphology. In addition, samples at the five different nominal compositions were characterized to determine any impact of the mixed-halide composition beyond tuning the bandgap. First-principles calculations were used to predict the formation energies and energy band structures of different crystal configurations. Specifically, the firstprinciples simulations shed light on structural hypotheses regarding the preferred distribution of Br- and I- anions in the alloyed samples and their connection to experimentally observed signatures.

RESULTS AND DISCUSSION Pure-Halide Crystal Structures

The pure-halide compositions are used as starting points for the exploration of the mixed-halide crystal structure. The $(PEA)_2PbI_4$ (x=0)⁵⁵⁻⁵⁷ and $(PEA)_2PbBr_4$ (x=1)^{58,59} crystal structures are known to consist of bilayers of PEA cations between single layers of corner sharing Pb-X octahedra. The $(PEA)_2PbI_4$ (x=0) structure used in this work is based on the $(PEA)_2PbI_4$ structure that was recently refined in detail and reported by Du *et al.*⁵⁵ (see **Supplementary Note I, Figure S1**, and **Tables S1-S2** for more information). The most stable $(PEA)_2PbBr_4$ structure is based on the structure from Shibuya *et al.*⁵⁸ (see **Supplementary Note I, Figures S2-S4** and **Tables S3-S4** for more information).

According to several experimental reports of (PEA)₂PbI₄ and (PEA)₂PbBr₄ atomic structures ⁵⁵⁻⁵⁹, the layered perovskites (PEA)₂PbI₄ and (PEA)₂PbBr₄ have different organic molecular stacking patterns, as shown in **Figure 2**. The phenyl rings of PEA molecules within the same organic layer align in the same direction for the (PEA)₂PbI₄ structure (Figure 2a), while the molecules align in different directions in (PEA)₂PbBr₄ (Figure 2b). The pure halide structures shown in Figure 2 are computationally derived structures, using the experimentally reported (XRD) structures of (PEA)₂PbI₄ by Du et al..55 and (PEA)₂PbBr₄ by Shibuya et al.58 as starting points. The pure-halide structures were optimized to reflect local minimum-energy structures according to van der Waals corrected semi-local density-functional theory (DFT). Specifically, the Perdew-Burke-Ernzerhof (PBE) exchange-correlation functional⁶⁰ was used, to which the Tkatchenko-Scheffler (TS) pairwise dispersion correction⁶¹ was added, referred to as DFT-PBE+TS in this work. The high-precision, all-electron code electronic structure FHI-aims⁶²⁻⁶⁶ was used as further detailed in the Methods section.

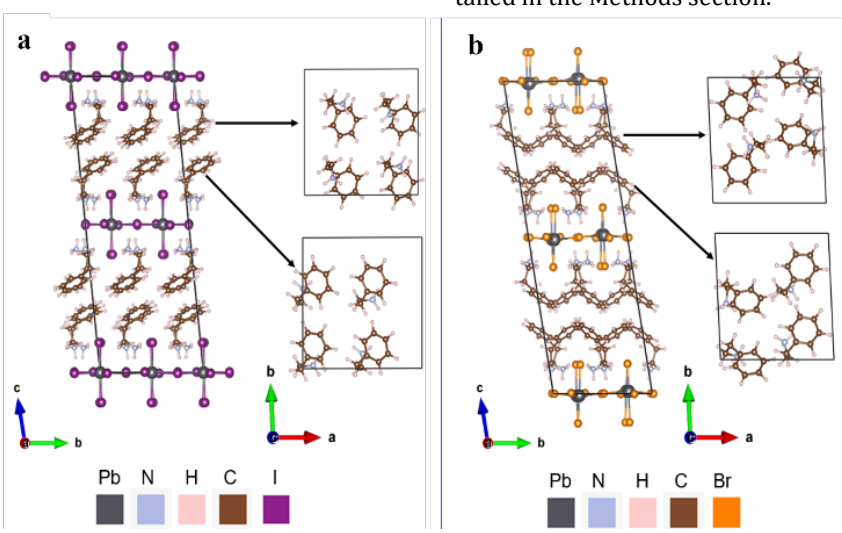


Figure 2. Pure Halide Crystal Structures. The most stable **(a)** (PEA)₂PbI₄ and **(b)** (PEA)₂PbBr₄ structures fully relaxed by DFT-PBE+TS. The insets show the orientation of organic layers for each structure seen in a top view along the c direction, which connects different organic/inorganic layers. The accompanying color scheme indicates the color used to represent the different chemical elements in each structure.

Two different molecular conformations were confirmed as lowest-energy structures among the ones considered for (PEA)₂PbI₄ and (PEA)₂PbBr₄, respectively. As is shown in the Supplementary Information (**Tables S2, S4-S5**), the actual structure parameters of the computationally optimized structures are very close to the experimentally determined structures, e.g., deviating by 1% or less from the T=100K (PEA)₂PbBr₄ crystal structures of Gong et al.⁵⁹ Importantly, the two different molecular arrangements found in (PEA)₂PbI₄ and (PEA)₂PbBr₄ are also distinct from a total energy point of view, as shown in Table S6. Switching the halide anion but not the molecular arrangement increases the computed total energy by 5 meV per halide atom (I substituted for Br in (PEA)2PbBr4 template structure) and 18 meV per halide atom (Br substituted for I in (PEA)₂PbI₄ template structure), respectively.

Mixed-Halide Film Composition

Turning to experimentally synthesized, mixed-halide films next, it is important to establish the degree of homogeneity achieved in mixed halide films deposited by RIR-MAPLE. Therefore, time-of-flight secondary ion mass spectrometry (TOF-SIMS) was used to characterize the depth profile of film composition in as-grown and annealed films. Figure 3 shows depth profiles of as-grown (a-e) and annealed (f-j) (PEA)₂Pb(I_{1-x}Br_x)₄ films for x = 0 (a & f), x = 0.25 (b & g), x = 0.5 (c & h), x = 0.75 (d & i), and x = 1 (e & j). The signal intensity corresponding to a specific molecule was measured to describe the film composition from the surface (depth = 0 nm) to the film-substrate interface (depth \approx 300 nm). Note that the intensity of the glass signature increases as the film depth approaches the film-substrate interface while the HOIP ionic signatures decrease.

Within each film, the intensities of PEA, lead, bromide, and iodide signatures remain fairly constant throughout the depth of the film. Additionally, the organic:inorganic intensity ratio (represented by PEA:Pb signatures) and the iodide:bromide intensity ratio remain constant throughout the depth of the film. These constant trends indicate that

none of the film constituents (organic cation, inorganic cation, or halide anion) segregate to the film surface, and each film is compositionally well-mixed throughout the film depth. Further, the TOF-SIMS spectra and energy dispersive spectroscopy (EDS) measurements (Figure S6) for the x = 0 and x = 1 films confirm that halide cross contamination does not occur between different RIR-MAPLE film deposition sessions. Specifically, for the TOF-SIMS spectra in Figure 3a & Figure 3f, the intensity of the bromide signature is lower than the iodide signature intensity by a factor of 104 and is less than 10 (i.e., within the measurement noise floor). This indicates that no bromide was detected in the x = 0 films. Similarly, Figure 3e & Figure 3j show iodide signature intensities in the measurement noise floor that are orders of magnitude below the bromide signature, indicating no iodide is present in the x = 1films. From the EDS spectra, Figure S6a confirms no bromide peak ($\sim 1.5 \text{ keV}$) is observed in the x = 0 films and no iodide peak ($\sim 3.9 \text{ keV}$) is observed in the x = 1 films.

The TOF-SIMS spectra and EDS measurements also confirm that the iodide-to-bromide ratio homogeneity was achieved in each mixed-halide film deposited by RIR-MAPLE. The bromide signature intensity (for depth \approx 0-300 nm) increases with increasing bromide content (x) from less than 10 a.u. (x = 0, Figure 3a & Figure 3f) to greater than 10^4 a.u. (x = 1, Figure 3e & Figure 3j). Likewise, the iodide signature intensity (for depth $\approx 0-300$ nm) decreases with increasing bromide content (x) from greater than 10^5 a.u. (x = 0, Figure 3a & Figure 3f) to less than 10 a.u. (x = 1, Figure 3e & Figure 3j). The EDS spectra in Figure S6a show the bromide signature peak intensity increasing and the iodide signature peak intensity decreasing with increasing bromide content. In addition, the EDS maps shown in Figure S6b demonstrate that, on the tens of microns scale of the measurement, the films are well mixed such that the iodide and bromide ions are dispersed homogeneously throughout the films.

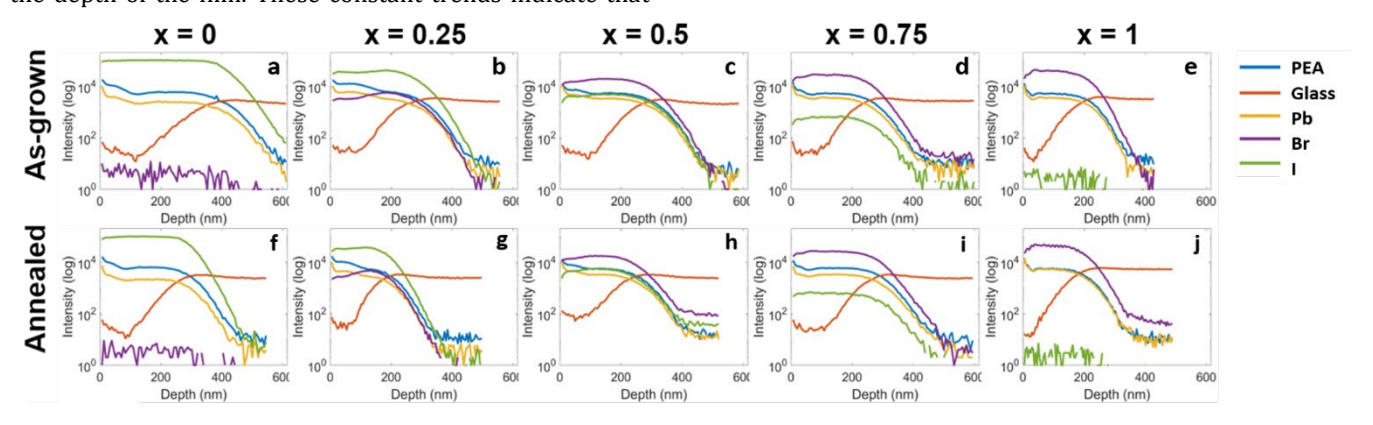


Figure 3. TOF-SIMS. TOF-SIMS depth profiles of (a) - (e) as-grown and (f) - (j) annealed $(PEA)_2Pb(I_{1-x}Br_x)_4$ films deposited by RIR-MAPLE for x = 0, 0.25, 0.5, 0.75, and 1. Note that the intensity is shown in arbitrary units (a.u.). Also note that the depth at which the signal for the glass substrate (red) becomes dominant seems to shift towards lower values after annealing ((a) & (f) and (b) & (g)), suggesting that the film may shrink. If the films were extremely smooth, the TOF-SIMS could indicate such a change; however, RIR-MAPLE films are generally rough²¹ and the TOF-SIMS depth profile does not give a definitive answer on this point.

Lastly, there are no significant differences in the TOF-SIMS molecular signature intensities or depth profiles between respective as-grown (Figures 3a-e) and annealed (Figures 3f-i) films. Similarly, the EDS measurements (Figure **S6**) reveal no significant differences between as-grown and annealed films. Thus, post-growth annealing does not affect the mixed-halide composition throughout the depth of the film. This observation is important to establish that RIR-MAPLE produces compositionally well-mixed films, and material does not precipitate out of the film or accumulate at the surface of the film (also confirmed with XRD, vide infra). These results also mean that the effects of postgrowth annealing on the structural and optical properties of films can be isolated and probed because controlled compositions were achieved as-grown and maintained after annealing.

Grazing incidence wide-angle X-ray scattering (GIWAXS) was used to probe the perovskite-phase purity of each film. **Figure 4a & Figure 4b** show the respective GIWAXS maps for as-grown and annealed (PEA)₂PbI₄ films (x = 0) deposited by RIR-MAPLE. The q values for the diffraction rings agree very well between the as-grown (**Figure 4a**) and annealed (**Figure 4b**) (PEA)₂PbI₄ film maps, such as the innermost ring that corresponds to the (002) reflection at q = 0.37 Å-¹. This agreement between the as-grown and annealed films is consistent for each subsequent reflection as evidenced by the rings at higher q values. For all film

compositions and regardless of annealing, there is some crystallographic texture along (00L). GIWAXS was also used to observe the film during post-growth annealing to capture the evolution of film crystallinity in time, as opposed to only before (as-grown, Figure 4a) and after (annealed, Figure 4b) heat treatment. Figure 4c shows GIWAXS measurements taken while increasing annealing temperature over time on an in-situ heating stage to detect any changes in the position, q, and intensity of each reflection. Aside from small decreases in q consistent with thermal expansion during the annealing process, the 2D perovskite (002) reflections remained steady. Further, the position and intensity of q were maintained consistently for all other film compositions, x = 0.25, 0.5, 0.75, and 1 (Figure S7 & Figure 4d). Figure 4d further supports composition control by the gradual change of the $\{002\}$ and $(1\overline{11})$ positions with increasing bromide compositions. Note that the shift is more pronounced for the $(1\overline{1}\overline{1})$ position compared to the change in the {002} positions because the (002) plane spacing depends mostly on the organic molecule in the 2D perovskites with less contribution from the halide. In contrast, for the $(1\overline{1}\overline{1})$ plane, the $[PbX_6]^{2-}$ octahedra significantly impact the in-plane contribution. As X goes from I- to Br- the octahedra expands significantly, thereby imposing a larger impact on the in-plane shift compared to the change in the out-of-plane direction.

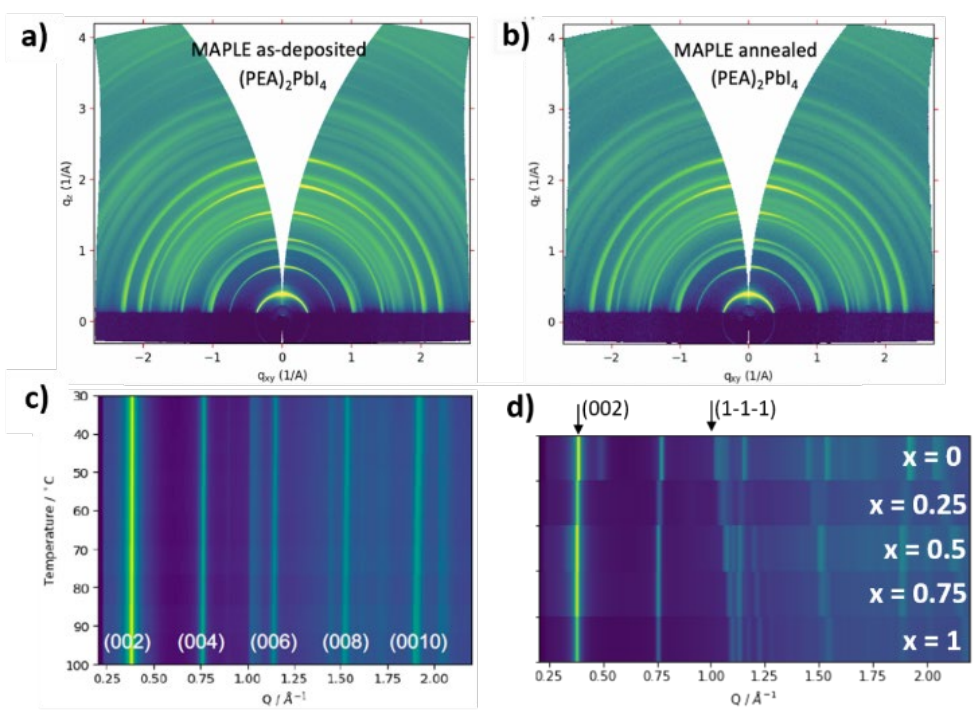


Figure 4. GIWAXS. GIWAXS measurements for x = 0 films **(a)** as-grown and **(b)** annealed. **c)** GIWAXS measurements of (PEA)₂PbI₄ during annealing on the GIWAXS stage from 30 °C to 100 °C at a rate of 1 °C per second. **d)** Stacked GIWAXS measurements for (PEA)₂Pb(I_{1-x}Br_x)₄ films with x = 0, 0.25, 0.5, 0.75, and 1 taken during annealing on the GIWAXS stage (from 30 °C to 110 °C at a rate of 1 °C per second for each composition).

Post-Growth Annealing

Overall, the GIWAXS patterns of as-grown and annealed films for each composition were indistinguishable (Figure **S7**), indicating that only the perovskite phase is formed without significant presence of intermediate or solvent complexes or any other secondary phases. It is important to note that Quintero *et. al* found that solvent complexes and other non-perovskite peaks were present in asdeposited films of solution-processed, quasi-2D HOIPs, namely $(PEA)_2MA_{n-1}Pb_nI_{3n+1}$. These non-perovskite phases disappeared by the end of annealing, indicating that heat treatment is crucial for reduced-dimensional metal halide perovskite formation using conventional methods.³⁶ In contrast, this work demonstrates that RIR-MAPLEdeposited (PEA)₂Pb(I_{1-x}Br_x)₄ films show similar crystallinity in both as-grown and annealed films, and post-growth annealing is not required to achieve perovskite-phase pure films of the PEA-based 2D HOIPs. The rings in the GIWAXS images shown in Figure S7 demonstrate that the crystallites in RIR-MAPLE films are randomly oriented with respect to the substrate. Further, this primarily random orientation does not change with annealing. Nonetheless, scanning electron microscopy (SEM) (Figure S8) and atomic force microscopy (AFM) (Figure S9) images show that post-growth annealing has a clear morphological effect on the (PEA)₂Pb(I_{1-x}Br_x)₄ films deposited by RIR-MAPLE. As an example, the x = 1 AFM image in **Figure S9** shows that the shape of the morphological features is the same in as-grown and annealed films, but the average size of the surface features increases with annealing.

Higher resolution investigation of the crystal structure by X-ray diffraction (XRD) was used to reveal subtle effects of post-growth annealing (110 °C for 10 minutes) on RIR-MAPLE-deposited (PEA)₂Pb($I_{1-x}Br_x$)₄ thin films. The highest intensity peaks in the as-grown (**Figure 5a**) and annealed (Figure 5b) XRD spectra (shown on a log scale) are closely aligned with the {002} perovskite reflections, and no solvent complex or PbI2 precursor peaks are observed. Consistent with the GIWAXS measurements, these XRD spectra confirm that post-growth annealing is not required to remove solvent from the film or to initiate perovskite formation. The (0010) peaks were considered to detect smaller differences in phase behavior among compositions for as-grown and annealed films, as shown in Figure 5c & **Figure 5d**, respectively. The starkest difference between as-grown and annealed films is observed for the x = 0.25film. The as-grown x = 0.25 film has a single (0010) XRD peak at 27° (Figure 5c), but after annealing, this peak splits into two separate peaks (Figure 5d). One of the new peaks shifts to the left of the as-grown x = 0.25 (0010) peak to 26.77° and the other moves to the right of that position to 27.16°. Typically, such peak splitting demonstrates halide phase segregation in mixed halide 3D HOIPs, 26,27 indicating that the well-mixed x = 0.25 film (under as-grown conditions) separates into an iodide-rich phase and a bromide-rich phase upon annealing. Interestingly, the peak splitting does not occur for the other mixed-halide compositions (x = 0.5 and x = 0.75).

It is also important to note that after annealing, the (0010) peak shifts to slightly higher 2θ values for several compositions: x=0 shifts from 27.15° to 27.20° , x=0.5 shifts from 26.60° to 26.67° , x=0.75 shifts from 26.60° to 26.65° , and x=1 shifts from 26.65° to 26.70° (Figure 5c & Figure 5d). Because the perovskite forms during the RIR-MAPLE growth process, the observed XRD peak splitting and shifts are likely effects of annealing the film after the perovskite has fully formed. The inset in Figure 5d depicts a possible mechanism for the slight shift in 2θ , namely, some PEA cation reorientation and/or improved PEA cation organization due to annealing that causes the organic bilayer thickness to decrease by Δd , which leads to a similar decrease in the interlayer spacing, d, and corresponding increase in the 2θ positions of the $\{002\}$ XRD peaks.

Comparing as-grown to annealed films as a function of composition shows additional differences in film properties, such as crystallite size and microstrain. These properties were calculated from the XRD spectra in Figure 5a & Figure 5b using the Williamson-Hall method^{26,67} (see Figure S10) and are shown in Figure S11. In Figure S11a, the x = 0.25 films showed the largest difference in average crystallite size, with the as-grown film averaging 117 nm and the annealed film averaging 48 nm. While no consistent trend in crystallite size is observed as a function of composition or post-growth annealing, it is clear that annealing can change the average, as-grown crystallite size. Note that these sizes are along the c-axis, normal to the quantum well layers. In Figure S11b, smaller microstrain values are observed primarily in annealed films as opposed to the as-grown counterparts, suggesting that postgrowth annealing promotes structural relaxation. The microstrain difference between as-grown and annealed films is largest for the x = 0.25 case: 0.60% vs 0.10%, respectively. The large microstrain in the as-grown x = 0.25 film is likely due to incipient compositional separation related to the halide phase segregation observed in the annealed x = x0.25 film. Further, the larger difference in microstrain for x = 0.25 compared to other compositions, along with the reduced crystallite size (Figure S11), suggest a relaxation of the film whereby two distinct structural phases, with smaller crystallite sizes, comprise the relaxed state due to post-growth annealing.

To further investigate annealing effects on the perovskite crystal structure, films were annealed at a higher temperature of 150°C for 10 minutes and characterized by XRD (**Figure S12** & **Figure S13**). Annealing at higher temperature led to the development of non-perovskite XRD peaks (# and *) for (PEA)₂PbI₄ and all mixed halide compositions (**Figure S12a**): x = 0, x = 0.25, x = 0.5, and x = 0.75. The peaks at 13° and 39° (*) are characteristic of PbI₂, indicating degradation of the perovskite structure after annealing at 150°C . 68 PbI₂ peaks are observed for x = 0, 0.25, and 0.5, but not for x = 0.75 and 1 which have a greater bromide content. Also, PbBr₂ peaks are not observed for any

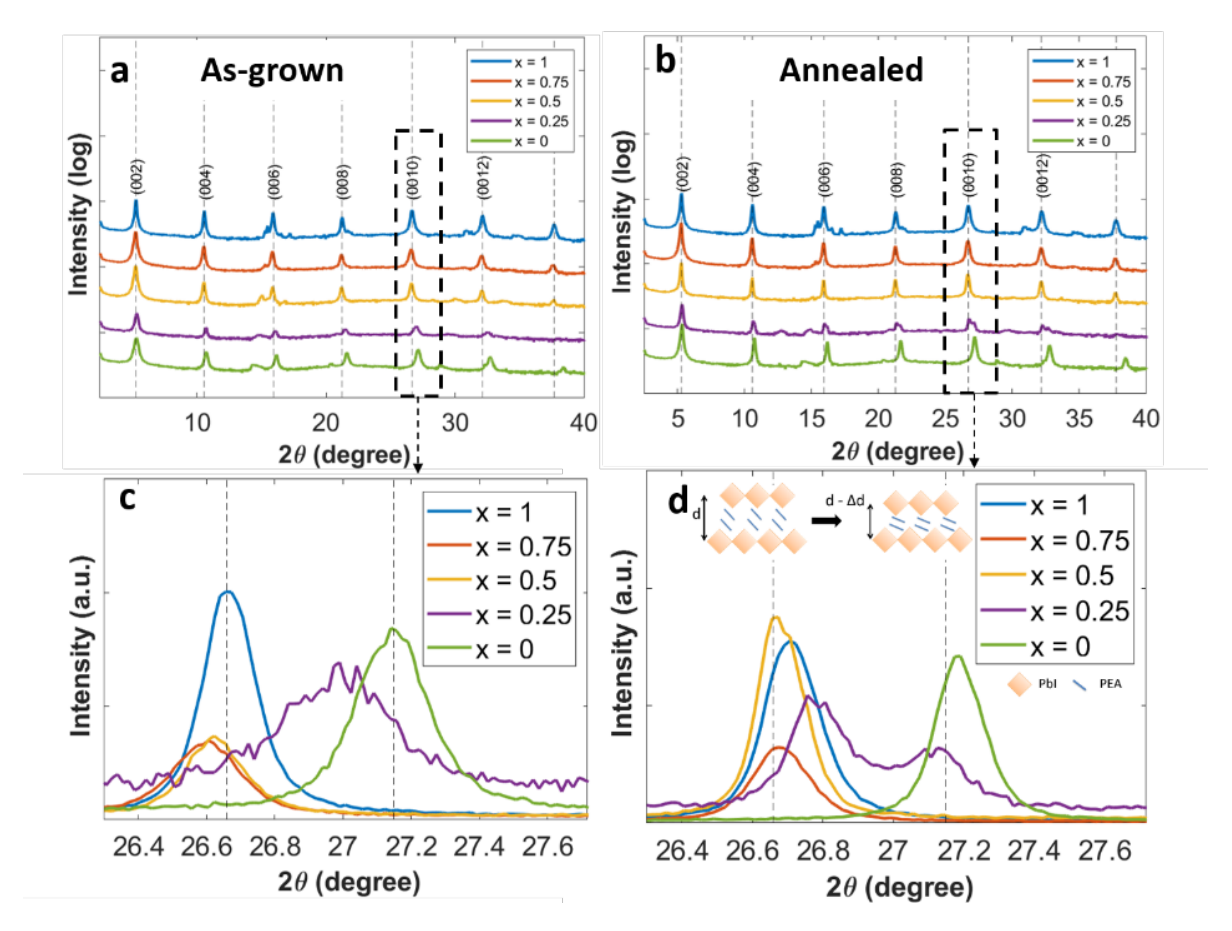


Figure 5. X-ray Diffraction. XRD spectra on a logarithmic scale for **(a)** as-grown and **(b)** annealed $(PEA)_2Pb(I_{1-x}Br_x)_4$ films. The (0010) XRD peaks for **(c)** as-grown and **(d)** annealed $(PEA)_2Pb(I_{1-x}Br_x)_4$ films. Dashed lines in **(a) & (b)** indicate $\{002\}$ reflections for as-grown and annealed x = 1 films, respectively. Dashed lines in **(c) & (d)** indicate the (0010) peak location for x = 1 and x = 0 as-grown films. **(Inset)** Schematic of PEA cation reorientation in $(PEA)_2Pb(I_{1-x}Br_x)_4$ films, where the PbI_6^{2-} is yellow and the PEA^+ cations are portrayed in blue.

composition or annealing condition, suggesting that bromine prefers to remain within the perovskite structure while iodine migrates. The peaks at 7° and 14° (#) are strongly characteristic of PEA-intercalated PbI₂.69 These non-perovskite peaks were most prominent in the x = 0.25film (**Figure 6a**). A closer look at the (0010) XRD peak for x = 0.25 (Figure 6b and Figure S13b) shows that while the (0010) peak becomes a single peak again at the higher annealing temperature (150°C), the corresponding 20 value decreases such that it is more aligned with the value expected for x = 1, (PEA)₂PbBr₄, Overall, annealing at higher temperature did not reverse the peak splitting in the x = 0.25 film such that it returned to the well-mixed state of the as-grown film. While the XRD peak splitting was only observed for the x = 0.25 film as a result of lowtemperature annealing at 110 °C, all three mixed-halide films showed peaks strongly characteristic of PEAintercalated PbI₂ after the higher temperature annealing, 150 °C (Figure S13b-d).

In order to explain the observations presented for the effects of post-growth annealing and mixed halide composition on 2D PEA-based HOIP films deposited by RIR-MAPLE, a possible crystal structure transformation is proposed. It is likely that during annealing, iodide escapes from the mixed-halide perovskite crystal structure (e.g., similar to Mosconi et al.70 and explained in reports by Boyd et al.71 and Wang et al.30). That the iodide leaves while bromide remains is plausible because perovskite crystal stability generally increases with bromide content.⁶⁹ Consequently, the iodide-based structure degrades into PEA-intercalated PbI₂. Therefore, the mixed-halide structure could degrade due to higher temperature annealing such that PbI2 XRD peaks⁶⁸ appear and the crystal forms an intercalated structure of PEA cations within PbI₂ sheets. Thus, the primary impact of post-growth annealing on (PEA)₂Pb(I_{1-x}Br_x)₄ thin films deposited by RIR-MAPLE is a combination of structural degradation and transformation.

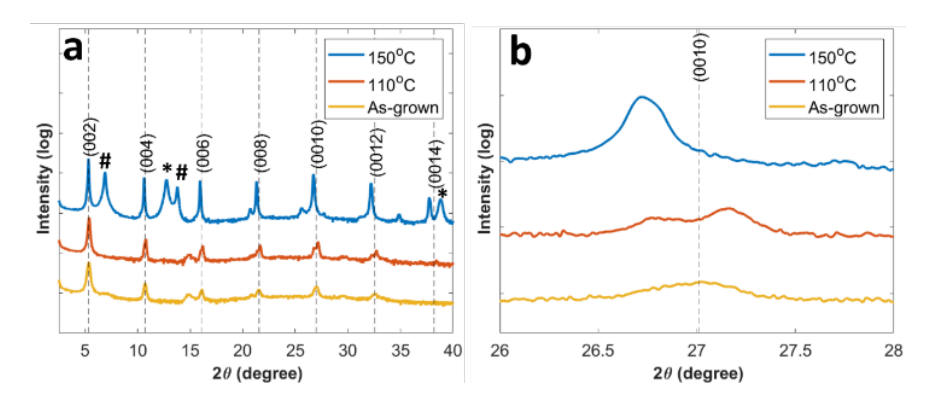


Figure 6. High Temperature Annealing Effects. (a) XRD spectra and **(b)** (0010) XRD peak of (PEA)₂Pb($I_{0.75}Br_{0.25}$)₄ films under different conditions: as-grown (unannealed), annealed at 110 °C for 10 minutes, and annealed at 150 °C for 10 minutes. (#) peaks are characteristic of PEA-intercalated PbI₂ and (*) peaks are characteristic of PbI₂. The dashed lines in **(a)** are aligned with the asgrown (002) reflection XRD peaks for reference. The dashed line in **(b)** is aligned with the as-grown x = 0.25 (0010) XRD peak for reference.

Mixed-Halide Crystal Structure

Determining whether the mixed-halide structures mimic either pure halide structure or are something entirely different is crucial to illustrate how these 2D mixed-halide HOIPs change due to annealing or composition. Firstprinciples total energy calculations of the alloy configurational space associated with the halide atoms were carried out to investigate the likely configurations of (PEA)2Pb(I1- $_{x}Br_{x}$)₄. Technical specifics of the first-principles assessment are provided in the Methods section. Two different molecular configurations were considered as starting points for mixed-halide model structures at x = 0.25, 0.5, and 0.75, namely the two distinct molecular arrangements of the pure halide endpoint structures (PEA)₂PbI₄ (x = 0) and $(PEA)_2PbBr_4$ (x = 1) as shown in Figure 2. Since $(PEA)_2PbI_4$ and (PEA)₂PbBr₄ prefer different organic stacking patterns and the nature of their cross-over as a function of halide composition is unknown, both the (PEA)2PbI4 and (PEA)₂PbBr₄ structures' organic stacking patterns were used as templates, individually, to build the mixed halide crystal structures. The $(2 \times 2) \times 2$ template unit cell (Figure S5d) was used, which can represent the unit cell of both the (PEA)₂PbBr₄ and of the (PEA)₂PbI₄ end point structures. The $(2 \times 2) \times 2$ unit cell has 376 total atomic sites, 40 of which can be occupied by halide atoms. The mixed halide crystal structure configuration space was constrained to have the same halide pattern in each inorganic layer of the $(2 \times 2) \times 2$ unit cells, i.e., assuming spatial homogeneity and neglecting the possibility of Br-I separation in adjacent planes. Each individual inorganic plane has two different types of halide sites, namely an equal number of equatorial (eq.) ones and axial (ax.) ones, as shown in Figure 7(c). It is conceivable that there might be a preference for either eq. or ax. sites by different halide anions. To evaluate this hypothesis, three different types of halide site configurations were considered in the computational models:

- (1) "Br \rightarrow Ax." denotes configurations in which the bromine atoms preferentially occupy the axial sites. For x = 0.25 and 0.5, such configurations do not require any Branions to reside in equatorial sites. For x = 0.75, all axial sites are filled with Brand, additionally, half of the equatorial sites are occupied by Brand.
- (2) "Br \rightarrow Eq." denotes configurations in which the bromine atoms preferentially occupy the equatorial sites. For x = 0.25 and 0.5, such configurations do not require any Branions to reside in axial sites. For x = 0.75, all equatorial sites are filled with Brand, additionally, half of the axial sites are occupied by Brand.
- (3) "Br \rightarrow Ax./Eq." denotes configurations in which Br⁻ and I⁻ configurations are evenly distributed between equatorial and axial sites.

In total, sixty-eight distinct (PEA)₂Pb(I_{1-x}Br_x)₄ configurations were considered, explained in detail in **Supplementary Note II** and illustrated in **Figure S14**.

Based on the aforementioned configurations, a formation energy diagram was calculated to provide insight into the mixed-halide structures that are most likely to occur (**Figure 7**). The first-principles total energy (E_{tot}) of each mixed-halide structure was obtained for fully optimized DFT-PBE+TS and then used to compute the formation energy (E_{form}) of each mixed-halide configuration, using the experimentally known end point structures as a reference. Considering that there are 40 halide sites in the (2 × 2) × 2 unit cell, the following equation was used to calculate the formation energy (E_{form}) of each proposed structure configuration:

$$\frac{E_{form}(x)}{halide\ atom} = \frac{\left[E_{tot}(x) - x \times E_{tot}(x=1) - (1-x) \times E_{tot}(x=0)\right]}{40} \tag{1}$$

In Equation 1, $E_{tot}(x)$ is the total energy of (PEA)₂Pb(I₁ $_x$ Br $_x$)₄ where x is the bromide content (0, 0.25, 0.5, 0.75, or 1). $E_{tot}(x=1)$ is the total energy of (PEA)₂PbBr₄ and $E_{tot}(x=0)$

is the total energy of (PEA)2PbI4. Each point in the formation energy diagram in Figure 7 represents a different possible structure configuration for the corresponding mixed-halide composition. The mixed-halide structures using the (PEA)₂PbI₄ and (PEA)₂PbBr₄ templates are shown in red and blue, respectively. For each template, mixed halide configurations structures in the three subsubspaces, Br \rightarrow Eq., Br \rightarrow Ax., and Br \rightarrow Eq./Ax., are represented by diamond, circle, and triangle points, respectively. The zero-energy line at 0 meV/atom connects the endpoints of the two pure halide compositions, x = 1 and x = 0. The formation energy diagram shows that the lowest energy structures are from the "Br \rightarrow Eq." subspace and they are based on the (PEA)₂PbBr₄ template. Thus, Br⁻ prefers to occupy the equatorial sites, qualitatively in line with the larger radius of I-, which likely finds lower-strain positions at the axial sites. A similar result for preferential bromine orientation was observed by Brivio et al.72 for the mixedhalide methylammonium structure, MAPb(Br_xI_{1-x})₃.

Interestingly, the formation energy diagram in **Figure 7** is fully consistent with the observation that XRD peak splitting, after annealing, occurs in the x=0.25 films but not in the x=0.5 or x=0.75 films. Specifically, the convex hull of the computed formation energies (green line in **Figure 7**) includes individual alloy configurations at the x=0.5 or x=0.5 or

0.75 as ground states. In contrast, none of the alloy configurations considered here reach the convex hull at x = 0.25. This means that, within the configuration space considered here, the thermodynamic ground state of the system at x =0.25 is the phase-separated limit of distinct domains of $(PEA)_2Pb(I_{1-x}Br_x)_4$ with x = 0 and x = 0.5. In other words, the x = 0.25 is more likely to segregate into I-rich and Brrich domains than the x = 0.5 and x = 0.75, for the configurations considered. This computational result is consistent with the experimental XRD spectra in which peak splitting only occurs for x = 0.25 (Figure 5d and Figure 6b). In contrast, the x = 0.5 and 0.75 structures show negative formation energies that sit on the convex hull, suggesting that the structures are unlikely to segregate into I-rich and Brrich domains. It is important to note that the diagram in **Figure 7** does not include finite-temperature effects, e.g., associated with the vibrational or configurational entropy. Furthermore, the energy difference between the lowestenergy microscopically mixed x=0.25 alloy configuration and the convex hull in Figure 7 is very small, consistent with the idea that a long-term metastable x=0.25 mixed alloy configuration may initially form and would only phase-segregate into the thermodynamically slightly more advantageous form of separate domains after annealing

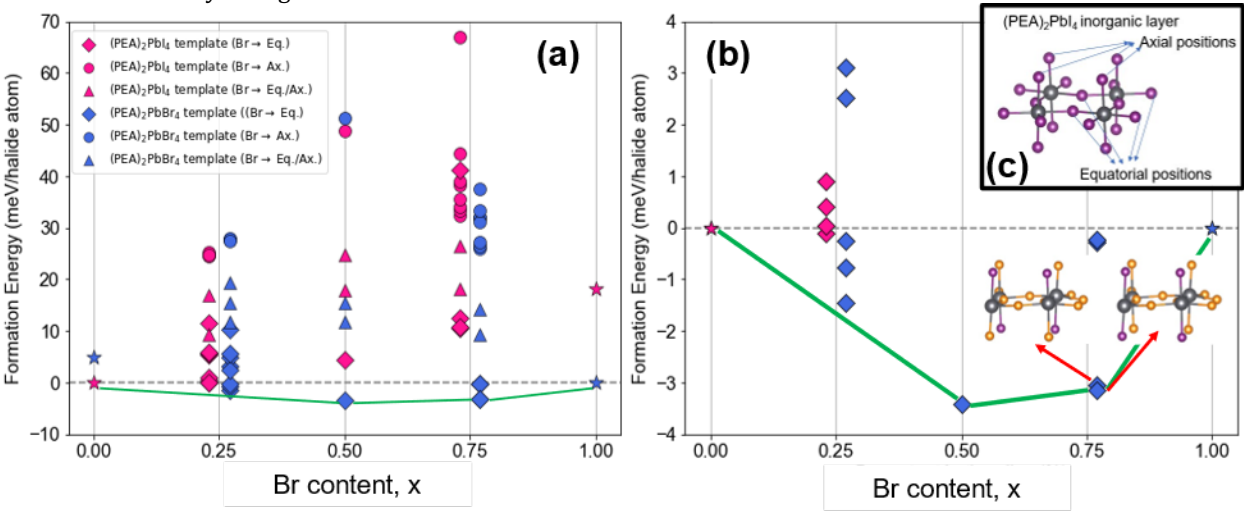


Figure 7. Formation Energy Diagram. a) Formation energies of fully relaxed (PEA)₂Pb($I_{1-x}Br_x$)₄ structures calculated by DFT-PBE+TS. b) Zoomed formation energy diagram of the lowest-energy configurations found. Inset in **b)** Two degenerate lowest-energy configurations of (PEA)₂Pb($I_{0.25}Br_{0.75}$)₄. **c)** Definition of equatorial and axial halide positions in a single inorganic layer of (PEA)₂PbI₄. In the atomic structure cartoons, I atoms are shown as purple spheres, Br atoms as orange spheres, and Pb atoms as grey spheres, while the molecules are omitted for visual clarity. In **(a)** and **(b)**, data points for mixed-halide structures based on the x = 0 template are shown in red and corresponding data points for structures based on the x = 1 template are blue. Note that energy points for the mixed-halide compositions x = 0.25 and x = 0.75 are slightly offset from the corresponding Br content line to clearly show all of the data points. For each template, mixed halide configurations structures in the three sub-subspaces, $Br \rightarrow Eq.$, $Br \rightarrow Ax.$, and $Br \rightarrow Eq./Ax.$ configurations as defined in the text are represented by diamond, circle, and triangle points, respectively. (The atomic structures of the lowest energy structures of (PEA)₂Pb($I_{1-x}Br_x$)₄ for x = 0.25, 0.5, and 0.75 can be found in the HybriD³ database of organic-inorganic semiconductors at https://materials.hybrid3.duke.edu under data set ID numbers 1905 (x = 0.25), 1906 (x = 0.5), 1907 (x = 0.75), 1908 (x = 0.75). The end point structures (x = 0 and x = 1) are also in the database under data set ID 1901 & 1902 (x = 0) and 1900 & 1903 (x = 1). These structures are included in the SI as well.)

Emission and Absorbance Properties

Overall, the optical properties of (PEA)₂Pb(I_{1-x}Br_x)₄ films deposited by RIR-MAPLE shown in Figure 8 demonstrate the expected tunability of the bandgap based on the mixedhalide composition. The excitonic photoluminescence (PL) peaks for the as-grown and annealed films for the x = 0 and x = 1 compositions are essentially the same (for each composition, respectively) with minimal differences in the FWHM linewidths. For the x = 0.25, x = 0.5, and x = 0.75compositions, the annealed film PL peaks are blue-shifted compared to the as-grown counterparts. However, in each case, the Stokes shift decreases upon annealing because the corresponding absorbance peaks red-shift compared to the as-grown absorbance peaks. When compared to the pure iodide and pure bromide films, the mixed halide films (both as-grown and annealed for x = 0.25, 0.5, and 0.75) have larger Stokes shifts. The larger Stokes shifts indicate that the mixed-halide films undergo greater energy losses during excitation than either pure halide structure. In addition, the FWHM linewidth of the mixed-halide PL spectra increases with increasing bromide content. Because the Stokes shifts and FWHM linewidths do not trend monotonically with bromide content, the optical properties of the mixed halide films provide additional experimental evidence that the mixed-halide crystal structures do not reflect the expected properties of a simple, ideal random mixture.

Another important observation that warrants further discussion is the extremely broad PL spectrum of the x = 0.75films. The as-grown PL spectrum in **Figure 8** shows two distinct peaks at 2.8 eV and 2.5 eV (the latter of which becomes a shoulder for the low-temperature annealed film). Most likely, these PL features are not due to halide phase segregation because the XRD spectra (**Figure 5c & Figure 5d, Figure S13i**) show no evidence for segregation in the x = 0.75 film annealed at 110 °C. Also, halide segregation is not favorable because the lowest energy x = 0.75 structure sits on the convex hull, as shown in **Figure 7.** Interestingly, however, this study found two distinct Br/I configurations that are energetically degenerate at x=0.75 (shown as insets in **Figure 7b**). One possible hypothesis is therefore that the PL features are characteristic of two types of octahedra that exist simultaneously within the x = 0.75 structure and correspond to the two lowest energy x = 0.75crystal structures shown in Figure 7b (Inset). This hypothesis is further investigated by comparing the calculated bandgap of both configurations to the measured photoluminescence of x = 0.75. Specifically, the Heyd-Scuseria-Ernzerhof (HSE06) functional including spin-orbit coupling (HSE06+SOC) was used to predict the band structure for the two lowest-energy x = 0.75 structures (**Figure 9**). Indeed, two distinct band gap values, at 2.682 eV and 2.594 eV, are found for the two different configurations. Although the 0.1 eV band gap difference found in the hybrid DFT calculations is not as large as the experimentally observed difference of PL features at 2.817 eV and 2.541 eV in the x = 0.75 spectrum (**Figure 8**), it is nevertheless substantial. Unlike in the experiments, excitonic effects are not included in the calculations (more accurate many-body treatments such as the Bethe-Salpeter Equation based on the GW approximation are currently not yet affordable for the system sizes at issue here). Thus, the idea of two different types of Br/I decorated octahedra and/or two different, competing ordered structures at x=0.75 is certainly consistent with the band structure results obtained by hybrid DFT.

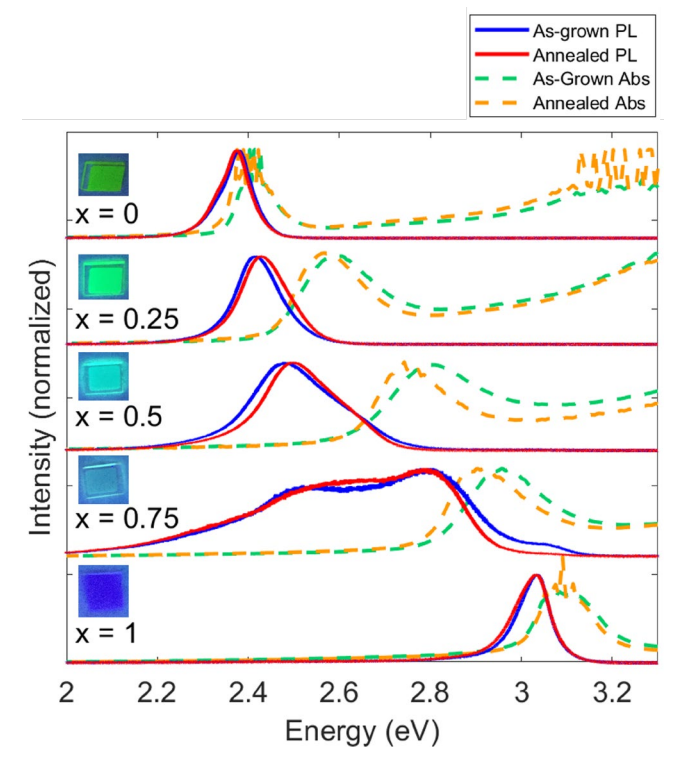


Figure 8. Photoluminescence and Absorbance. PL (solid lines) and UV-Vis absorbance (dashed lines) spectra of asgrown and annealed (PEA)₂Pb($I_{1-x}Br_x$)₄ films for x = 0, 0.25, 0.5, 0.75, and 1. (Inset) Photographs of films under UV excitation for each composition. Photographs of films under normal light are included in **Figure S15**.

To help explain the unique observations for the x = 0.75 PL spectra, the Heyd-Scuseria-Ernzerhof functional including spin-orbit coupling (HSE06+SOC) approach was used to predict the band structure for the two lowest-energy x = 0.75 structures determined corresponding to two kinds of Pb-halide octahedra (**Figure 9**). The two structures shown have direct band gaps at 2.682 eV and 2.594 eV, which possibly explains the experimentally observed PL features at 2.817 eV and 2.541 eV in the x = 0.75 spectrum (**Figure 8**).

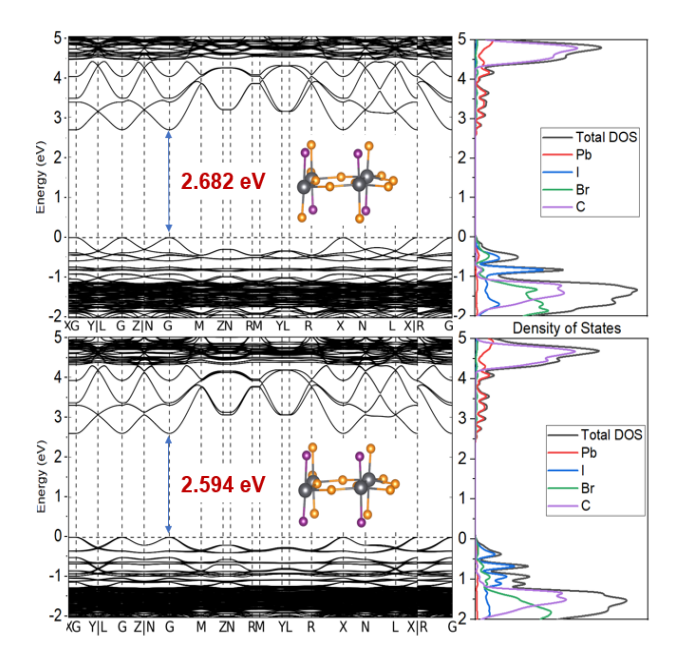


Figure 9. Band Structure for x = 0.75. Band structures and species projected density of states (DOS) of the two lowest-energy (PEA)₂Pb($I_{0.25}Br_{0.75}$)₄ structures, calculated by DFT-HSE06+SOC.

CONCLUSIONS

In summary, RIR-MAPLE produced high-quality crystalline phases of mixed-halide PEA based layered perovskites – (PEA)₂Pb(I_{1-x}Br_x)₄ for x = 0, 0.25, 0.5, 0.75, and 1 – in a facile thin film deposition process. Surprisingly, post-growth annealing is not required to achieve these compositionally well-mixed and perovskite phase-pure films (as demonstrated by the TOF-SIMS, EDS, and GIWAXS characterizations). In fact, XRD analysis revealed that post-growth annealing (especially at higher temperatures) is detrimental in that it promotes degradation and/or halide phase segregation.

First principles calculations show good agreement between computationally predicted and experimentally known crystal structures of the pure end point compositions (x = 0 and x = 1). Furthermore, the molecular arrangement associated with (PEA)₂PbBr₄ is energetically preferred for x = 0.25, 0.5, and 0.75, and only the (PEA)₂PbI₄ end point structure shows a different molecular arrangement. In the inorganic layers, bromine prefers to occupy equatorial positions in the Pb-X octahedra as opposed to the axial positions.

Regarding miscibility, the alloyed structures are predicted to be energetically preferred for x=0.5 and x=0.75, whereas a weak miscibility gap around x=0.25 results in the computations. The predictions were consistent with experimental data showing that, after post-growth annealing, XRD peak splitting occurred for the x=0.25 film but not the x=0.5 or x=0.75 films indicating some halide phase segregation in the x=0.25 film.

Moreover, the PL spectrum for the x=0.75 had two features while the x=0.25 and x=0.5 spectra only had one peak each. The theoretical band structure for the x=0.75 film supported the hypothesis that the two features in the PL spectra might be characteristic of two different but similarly likely x=0.75 crystal configurations simultaneously present in the film.

The key finding of this study is that one must consider the distinct site and ordering preferences of n = 1 mixed-halide perovskites in order to understand and rationally tune their properties. The miscibility gap observed around x =0.75 correlates directly with the preference of the larger Ianions to occupy axial rather than the spatially more constrained equatorial sites, coupled with the different molecular orientation preferences that distinguishes the pure iodide phase (x = 0) from the bromide containing phases (x = 0) \geq 0.5). Likewise, distinct I- configurations on the axial sites are preferred over others for x = 0.75 and can shape the observed optoelectronic properties. Without considering these preferences, one would miss the key driving force that shapes the materials' properties as they age and evolve to their thermodynamically preferred configurations. Overall, RIR-MAPLE was critical to enable isolation of post-growth annealing effects from compositional effects on the mixed-halide crystal structures to elucidate this nuanced behavior in the 2D mixed-halide HOIPs.

EXPERIMENTAL METHODS

Materials

The organic salts, phenethylammonium iodide ($C_8H_{12}IN$, >99% purity) and phenethylammonium bromide ($C_8H_{12}BrN$, >99% purity), were purchased from Sigma-Aldrich Corp. (now MilliporeSigma). The metal halides, lead (II) iodide (PbI_2 , 99.999% purity) and lead (II) bromide ($PbBr_2$, 99.999% purity), were purchased from Tokyo Chemical Industry Co., Ltd. (TCI). Anhydrous dimethyl sulfoxide (DMSO) and anhydrous monoethylene glycol (MEG) were purchased from Sigma-Aldrich Corp. (now MilliporeSigma). Soda-lime glass substrates were purchased from VWR International, LLC. All materials were used as received without further purification.

Perovskite Thin Film Fabrication

Thin films of $(PEA)_2Pb(I_{1-x}Br_x)_4$ were grown from 22mM precursor solutions using resonant infrared, matrix-assisted pulsed laser evaporation. The target solutions were comprised of (PEA)I, (PEA)Br, PbI_2 , and $PbBr_2$ in 1:1 DMSO:MEG by volume. The solutions were mechanically mixed at room temperature for approximately 5 minutes until the precursor materials were visibly dissolved in the solvents. The substrates were 2 cm x 2 cm of SiO_2 glass. The solution is placed into the target cup in the growth chamber and cooled to $-196^{\circ}C$ under vacuum (approx. 2 e-5 Torr). Once the target solution is frozen, an Er:YAG laser (2.94 μ m) is used to remove the top layer of the frozen target that is primarily solvent. Regarding the frozen target, it is unlikely that the precursors react in solution to

form perovskite clusters or nanoparticles prior to freezing because a film formation study has shown that perovskite is not present in the film until at least 10-40 minutes of deposition by RIR-MAPLE. 48,73 Thus, the laser rasters back and forth across the surface of the frozen target to sublimate the MEG in the solution, ejecting the precursor material up onto the substrate spinning in the holder 7 cm above the target cup. The substrate temperature is not controlled and remains at approximately 10°C while in the cooled growth chamber. Each film was deposited in the growth chamber for 4 hours, and then transferred to the load lock. The samples remained in the load lock under turbo vacuum (2 e-5 Torr) for 1 hour before being removed from the RIR-MAPLE system. The as-grown films were completed at that time and measured using XRD. The annealed films were annealed at 110°C for 10 minutes on a hot plate in an N₂ environment before being transferred to the XRD stage for measuring.

Time-of-Flight, Secondary Ion Mass Spectrometry (TOF-SIMS)

TOF-SIMS measurements were taken on a ION-TOF TOF-SIMS V instrument using standard profiling and the MCs+ method. 74,75 For standard profiling, the beam resolution is around 3-5 microns, but still large scale lateral variation in some species can be observed in this mode if they are present. Measurements were taken over a 50 x 50 um² analysis area using a 30 keV Bi3+ primary ion beam, and a 1 keV Cs sputter beam rastering over a 150 µm x 150 µm area. Measurements were completed by profiling from the top surface of the film (x = 0 nm) down through the depth of the film past the substrate/film interface at approximately x = 300 nm. The MCs+ method is outlined by Harvey *et al.* and uses clusters of iodine and bromine with cesium from the sputter beam for enhanced halide sensitivity in positive polarity. In this work, the secondary ion cluster Cs₃Br₂ is reflective of Br+ and Cs3I2 reflects I+; each cluster has a higher signal than just the respective halide ion peak. C₂H₃+ clusters were measured to track the PEA in the film. Si+ reflects the SiO₂ glass substrate, and Pb+ reflects the lead in the film.

Grazing Incidence Wide Angle X-ray Scattering and X-ray Diffraction

GIWAXS measurements were taken of 1 x 1 cm² samples using beam line 11-3 of Stanford Synchrotron Radiation Lightsource (SSRL) at the SLAC National Accelerator Laboratory. The source has an energy of 12700 eV and 0.15 x 0.05 mm spot size. A 73.242 μ m x 73.242 μ m Raxyonics 225 detector was used. *In-situ* GIWAXS measurements were taken while the films were annealed on the GIWAXS stage from 30° to 100°C at a rate of 1°C per second. The *in-situ* measurements took approximately 90 seconds during which time the samples remained on the stage in a helium environment. Each film was only heated once to mimic the post-growth annealing process during annealed film fabrication process. Igor Pro with NIKA and WAXStools were used to process and analyze the data.

XRD spectra were acquired using a Panalytical Empyrean X-ray diffractometer with Cu K- α radiation. The operating voltage was 45 kV and the current was 40 mA. Continuous scans were taken from 2.5 to 70 degrees.

Energy Dispersive X-ray Spectroscopy (EDS)

Energy dispersive x-ray spectroscopy measurements were taken at SLAC National Accelerator Laboratory using the Stanford Synchrotron Radiation Lightsource (SSRL).

Scanning Electron Microscopy and Atomic Force Microscopy

Scanning electron microscopy (SEM) images were acquired using an Apreo S system by ThermoFisher Scientific. The accelerating voltage was 2 kV and the beam current ranged from 25 pA to 1nA in order to improve the image quality. Secondary ions were detected using an Everhart-Thornley detector. Atomic force microscopy (AFM) images were taken using a Digital Instruments Dimension 3100 system by Bruker. Films on 1 cm x 1cm glass substrates were placed onto the instrument stage in an ambient air environment for imaging. The images were taken of 5 μm x 5 μm areas in several different locations on the film. Tapping mode was used to limit contact between the tip and the film. AFM images were then processed using Gwyddion software.

UV-Vis Absorption and Photoluminescence

Ultraviolet-visible (UV-Vis) absorption spectra were acquired using a Shimadzu UV-3600 spectrophotometer. Samples of films on glass substrates were measured. Photoluminescence (PL) spectroscopy measurements were taken using a Horiba Jobin Yvon LabRam ARAMIS system. All films were excited using a 325 HeCd laser source with a 1% filter. Samples were kept in ambient air conditions for both sets of optical measurements.

First-Principles Calculations

The first-principles calculations were carried out with the high-precision, all-electron electronic structure code FHIaims. 62-66 In particular, this code enables large-scale, spinorbit coupled hybrid density functional calculations for energy band structures, needed in this work (see below). Unit cell sizes containing up to 376 atoms were considered, as explained in Figure S5. For all pure- and mixedhalide structures, atomic positions and lattice vectors were first computationally optimized using van der Waals corrected semi-local density-functional theory (DFT), until the structure corresponded to a local minimum of the Born-Oppenheimer potential energy surface. Specifically, the semilocal Perdew-Burke-Ernzerhof (PBE) exchangecorrelation functional⁶⁰ was combined with the Tkatchenko-Scheffler (TS) pairwise dispersion scheme⁶¹ to determine local minimum-energy structures and FHI-aims "intermediate" numerical defaults and 3×3×1 reciprocalspace grids were used. The usage of "intermediate" basis set and 3×3×1 reciprocal-space grids for structure optimization was validated by comparing with a more stringent parameter setting, "tight" basis set with 4×4×2 k-grids, as shown in **Table S5**. The deviation of lattice parameter between these two computational settings is less than 0.1 %, i.e., negligible. The magnitude of any residual energy gradient as a function of atomic position or lattice vector was required to be below 0.005 eV/Å. For the fully relaxed structures, energy band structures were calculated using the Heyd-Scuseria-Ernzerhof (HSE06) hybrid density functional^{76,77} including spin-orbit coupling (SOC) in a secondvariational approach that was extensively benchmarked in past work.63 The exchange mixing parameter of the HSE06 functional was fixed at 25% and the screening parameter was fixed at $\Omega = 0.11$ (Bohr radii)⁻¹. Using this fixed version of the parameters in the HSE06 density functional avoids a system-specific parameterization, retaining instead a single form that allows one to compare energy band structures across different structures in this work as well as in the literature⁷⁸⁻⁸¹. For the band structures, FHIaims' "intermediate" settings and dense k-point grids of 4×4×3 were used as done, e.g., in Liu et al.⁷⁸ The overall computational approach used here has been shown to yield results in excellent qualitative agreement with experimental observations in past work by some of this group. 49,78,80,82 The calculations used in this work's computational approach can be found in the NOMAD repository (https://nomad-lab.eu/prod/rae/gui/search?order=-1&order_by=authors&per_page=100&results=entries&vis

tion=elements&upload_id=nT82rxFGSgCZvD5aNaduiw).

ASSOCIATED CONTENT

Supporting Information

(PEA)₂PbBr₄ crystal structure literature search, EDS, GIWAXS, SEM, AFM, Williamson-Hall plots, crystallite size and microstrain, XRD at various temperatures for all compositions, theoretical mixed-halide structure configuration space and structures, Gaussian fits of PL spectra, and photos of films This material is available free of charge via the Internet at http://pubs.acs.org.

AUTHOR INFORMATION

Corresponding Authors

- * Niara E. Wright Duke University, Durham, NC, USA 27708; orcid.org/0000-0003-0896-1028; Email: niara.wright@duke.edu
- * Adrienne D. Stiff-Roberts Duke University, Durham, NC, USA 27708; orcid.org/0000-0001-6117-8943; Email: Adrienne.stiffroberts@duke.edu

Author Contributions

All authors have given approval to the final version of the manuscript.

Notes

The authors declare no competing financial interest.

ACKNOWLEDGMENTS

This work – namely all of the RIR-MAPLE growth, all materials characterization, all first principles calculations of mixed-halide (PEA) $_2$ Pb(I $_1$ - $_x$ Br $_x$) $_4$ structures and bandstructures – was funded by the Center for Hybrid Organic Inorganic Semiconductors for Energy (CHOISE) an Energy Frontier Research Center funded by the Office of Science, Office of Basic Energy Sciences within the U.S. Department of Energy.

N.E.W. acknowledges the Dean's Graduate Fellowship from Duke University and the Sloan Scholarship by Duke University Center of Exemplary Mentoring. The authors acknowledge D.B. Mitzi (Duke University) for helpful conversations and suggestions on XRD analysis.

The analysis of unalloyed (PEA)₂PbI₄ and (PEA)₂PbBr₄ structures from the literature and from first principles by X.Q. was supported by the National Science Foundation under Award Number DMR-1729297. This research used resources of the National Energy Research Scientific Computing Center (NERSC), a U.S. Department of Energy (DOE) Office of Science User Facility operated under Contract No. DEAC02-05CH11231.

Use of the Stanford Synchrotron Radiation Lightsource, SLAC National Accelerator Laboratory, is supported by the U.S. Department of Energy, Office of Science, Office of Basic Energy Sciences under Contract No. DE-AC02-76SF00515.

This work was authored in part by the National Renewable Energy Laboratory, operated by Alliance for Sustainable Energy, LLC, for the U.S. Department of Energy (DOE) under Contract No. DE-AC36-08G028308. The views expressed in the article do not necessarily represent the views of the DOE or the U.S. Government. The U.S. Government retains and the publisher, by accepting the article for publication, acknowledges that the U.S. Government retains a nonexclusive, paid-up, irrevocable, worldwide license to publish or reproduce the published form of this work, or allow others to do so, for U.S. Government purposes.

REFERENCES

- (1) Zhang, F.; Lu, H.; Tong, J.; Berry, J. J.; Beard, M. C.; Zhu, K. Advances in Two-Dimensional Organic-Inorganic Hybrid Perovskites. *Energy Environ. Sci.* **2020**, *13* (4), 1154–1186. https://doi.org/10.1039/c9ee03757h.
- (2) Zhang, F.; Kim, D. H.; Zhu, K. 3D/2D Multidimensional Perovskites: Balance of High Performance and Stability for Perovskite Solar Cells. *Curr. Opin. Electrochem.* **2018**, *11*, 105–113. https://doi.org/10.1016/j.coelec.2018.10.001.
- (3) Grancini, G.; Nazeeruddin, M. K. Dimensional Tailoring of Hybrid Perovskites for Photovoltaics. *Nat. Rev. Mater.* **2019**, 4 (1), 4–22. https://doi.org/10.1038/s41578-018-0065-0.
- (4) Cao, D. H.; Stoumpos, C. C.; Farha, O. K.; Hupp, J. T.; Kanatzidis, M. G. 2D Homologous Perovskites as Light-Absorbing Materials for Solar Cell Applications. J. Am. Chem. Soc. 2015, 137 (24), 7843–7850. https://doi.org/10.1021/jacs.5b03796.
- (5) Chen, P.; Bai, Y.; Wang, S.; Lyu, M.; Yun, J. H.; Wang, L. In Situ Growth of 2D Perovskite Capping Layer for Stable and Efficient Perovskite Solar Cells. Adv. Funct. Mater. 2018, 28 (17), 1706923. https://doi.org/10.1002/adfm.201706923.
- (6) Chen, A. Z.; Shiu, M.; Deng, X.; Mahmoud, M.; Zhang, D.; Foley, B. J.; Lee, S.-H.; Giri, G.; Choi, J. J. Understanding the Formation of Vertical Orientation in Two-Dimensional Metal Halide Perovskite Thin Films. *Chem. Mater.* 2019, 31 (4), 1336–1343.

- https://doi.org/10.1021/acs.chemmater.8b04531.
- (7) Grancini, G.; Roldán-Carmona, C.; Zimmermann, I.; Mosconi, E.; Lee, X.; Martineau, D.; Narbey, S.; Oswald, F.; De Angelis, F.; Graetzel, M.; Nazeeruddin, M. K. One-Year Stable Perovskite Solar Cells by 2D/3D Interface Engineering. *Nat. Commun.* **2017**, 8 (1), 15684. https://doi.org/10.1038/ncomms15684.
- (8) Jena, A. K.; Kulkarni, A.; Miyasaka, T. Halide Perovskite Photovoltaics: Background, Status, and Future Prospects. Chem. Rev. 2019, 119 (5), 3036–3103. https://doi.org/10.1021/acs.chemrev.8b00539.
- (9) Lee, H. D.; Kim, H.; Cho, H.; Cha, W.; Hong, Y.; Kim, Y. H.; Sadhanala, A.; Venugopalan, V.; Kim, J. S.; Choi, J. W.; Lee, C. L.; Kim, D.; Yang, H.; Friend, R. H.; Lee, T. W. Efficient Ruddlesden-Popper Perovskite Light-Emitting Diodes with Randomly Oriented Nanocrystals. Adv. Funct. Mater. 2019, 29 (27), 1901225. https://doi.org/10.1002/adfm.201901225.
- (10) Han, T. H.; Lee, J. W.; Choi, Y. J.; Choi, C.; Tan, S.; Lee, S. J.; Zhao, Y.; Huang, Y.; Kim, D.; Yang, Y. Surface-2D/Bulk-3D Heterophased Perovskite Nanograins for Long-Term-Stable Light-Emitting Diodes. Adv. Mater. 2020, 32 (1), 1905674. https://doi.org/10.1002/adma.201905674.
- (11) Ma, C.; Leng, C.; Ji, Y.; Wei, X.; Sun, K.; Tang, L.; Yang, J.; Luo, W.; Li, C.; Deng, Y.; Feng, S.; Shen, J.; Lu, S.; Du, C.; Shi, H. 2D/3D Perovskite Hybrids as Moisture-Tolerant and Efficient Light Absorbers for Solar Cells. *Nanoscale* 2016, 8 (43), 18309–18314. https://doi.org/10.1039/c6nr04741f.
- (12) Cai, P.; Wang, X.; Seo, H. J.; Yan, X. Bluish-White-Light-Emitting Diodes Based on Two-Dimensional Lead Halide Perovskite (C ₆ H ₅ C ₂ H ₄ NH ₃) ₂ PbCl ₂ Br ₂. Appl. Phys. Lett. **2018**, 112 (15), 153901. https://doi.org/10.1063/1.5023797.
- (13) Li, Z.; Chen, Z.; Yang, Y.; Xue, Q.; Yip, H. L.; Cao, Y. Modulation of Recombination Zone Position for Quasi-Two-Dimensional Blue Perovskite Light-Emitting Diodes with Efficiency Exceeding 5%. *Nat. Commun.* **2019**, *10* (1), 1027. https://doi.org/10.1038/s41467-019-09011-5.
- (14) Mitzi, D. B. Templating and Structural Engineering in Organic-Inorganic Perovskites. J. Chem. Soc. Dalt. Trans. 2001, No. 1, 1–12. https://doi.org/10.1039/b007070j.
- (15) Mitzi, D. B. Synthesis, Crystal Structure, and Optical and Thermal Properties of (C 4 H 9 NH 3) 2 MI 4 (M = Ge, Sn, Pb). *Chem. Mater.* **1996**, 8 (3), 791–800. https://doi.org/10.1021/cm9505097.
- (16) Saparov, B.; Mitzi, D. B. Organic-Inorganic Perovskites: Structural Versatility for Functional Materials Design. *Chem. Rev.* 2016, 116 (7), 4558–4596. https://doi.org/10.1021/acs.chemrev.5b00715.
- (17) Smith, M. D.; Connor, B. A.; Karunadasa, H. I. Tuning the Luminescence of Layered Halide Perovskites. *Chem. Rev.* **2019**, 119 (5), 3104–3139. https://doi.org/10.1021/acs.chemrev.8b00477.
- (18) Dunlap-Shohl, W. A.; Zhou, Y.; Padture, N. P.; Mitzi, D. B. Synthetic Approaches for Halide Perovskite Thin Films. *Chem. Rev.* **2019**, *119* (5), 3193–3295. https://doi.org/10.1021/acs.chemrev.8b00318.
- (19) Berhe, T. A.; Su, W. N.; Chen, C. H.; Pan, C. J.; Cheng, J. H.; Chen, H. M.; Tsai, M. C.; Chen, L. Y.; Dubale, A. A.; Hwang, B. J. Organometal Halide Perovskite Solar Cells: Degradation and Stability. *Energy Environ. Sci.* **2016**, 9 (2), 323–356. https://doi.org/10.1039/c5ee02733k.
- (20) Green, M. A.; Ho-Baillie, A.; Snaith, H. J. The Emergence of Perovskite Solar Cells. *Nat. Photonics* 2014, 8 (7), 506–514. https://doi.org/10.1038/nphoton.2014.134.
- (21) Dunlap-Shohl, W. A.; Barraza, E. T.; Barrette, A.; Gundogdu, K.; Stiff-Roberts, A. D.; Mitzi, D. B. MAPbI₃ Solar Cells with Absorber Deposited by Resonant Infrared Matrix-Assisted

- Pulsed Laser Evaporation. *ACS Energy Lett.* **2018**, *3* (2), 270–275. https://doi.org/10.1021/acsenergylett.7b01144.
- (22) Bush, K. A.; Palmstrom, A. F.; Yu, Z. J.; Boccard, M.; Cheacharoen, R.; Mailoa, J. P.; McMeekin, D. P.; Hoye, R. L. Z.; Bailie, C. D.; Leijtens, T.; Peters, I. M.; Minichetti, M. C.; Rolston, N.; Prasanna, R.; Sofia, S.; Harwood, D.; Ma, W.; Moghadam, F.; Snaith, H. J.; Buonassisi, T.; Holman, Z. C.; Bent, S. F.; McGehee, M. D. 23.6%-Efficient Monolithic Perovskite/Silicon Tandem Solar Cells with Improved Stability. Nat. Energy 2017, 2 (4), 1–7. https://doi.org/10.1038/nenergy.2017.9.
- (23) Jošt, M.; Bertram, T.; Koushik, D.; Marquez, J. A.; Verheijen, M. A.; Heinemann, M. D.; Köhnen, E.; Al-Ashouri, A.; Braunger, S.; Lang, F.; Rech, B.; Unold, T.; Creatore, M.; Lauermann, I.; Kaufmann, C. A.; Schlatmann, R.; Albrecht, S. 21.6%-Efficient Monolithic Perovskite/Cu(In,Ga)Se₂ Tandem Solar Cells with Thin Conformal Hole Transport Layers for Integration on Rough Bottom Cell Surfaces. ACS Energy Lett. 2019, 4 (2), 583–590. https://doi.org/10.1021/acsenergylett.9b00135.
- (24) NREL. Best Research-Cell Efficiency Chart | Photovoltaic Research | NREL https://www.nrel.gov/pv/cell-efficiency.html (accessed Feb 18, 2020).
- (25) Brennan, M. C.; Draguta, S.; Kamat, P. V.; Kuno, M. Light-Induced Anion Phase Segregation in Mixed Halide Perovskites. *ACS Energy Lett.* **2018**, *3* (1), 204–213. https://doi.org/10.1021/acsenergylett.7b01151.
- (26) Hoke, E. T.; Slotcavage, D. J.; Dohner, E. R.; Bowring, A. R.; Karunadasa, H. I.; McGehee, M. D. Reversible Photo-Induced Trap Formation in Mixed-Halide Hybrid Perovskites for Photovoltaics. *Chem. Sci.* 2015, 6 (1), 613–617. https://doi.org/10.1039/C4SC03141E.
- (27) Slotcavage, D. J.; Karunadasa, H. I.; McGehee, M. D. Light-Induced Phase Segregation in Halide-Perovskite Absorbers. *ACS Energy Lett.* **2016**, *1* (6), 1199–1205. https://doi.org/10.1021/acsenergylett.6b00495.
- Bischak, C. G.; Hetherington, C. L.; Wu, H.; Aloni, S.; Ogletree, D. F.; Limmer, D. T.; Ginsberg, N. S. Origin of Reversible Photoinduced Phase Separation in Hybrid Perovskites. *Nano Lett.* 2017, 17 (2), 1028–1033. https://doi.org/10.1021/acs.nanolett.6b04453.
- (29) Diez-Cabanes, V.; Even, J.; Beljonne, D.; Quarti, C. Electronic Structure and Optical Properties of Mixed Iodine/Bromine Lead Perovskites. To Mix or Not to Mix? Adv. Opt. Mater. 2021, 2001832. https://doi.org/10.1002/adom.202001832.
- (30) Wang, D.; Wright, M.; Elumalai, N. K.; Uddin, A. Stability of Perovskite Solar Cells. Sol. Energy Mater. Sol. Cells 2016, 147, 255–275. https://doi.org/10.1016/j.solmat.2015.12.025.
- (31) Meloni, S.; Moehl, T.; Tress, W.; Franckeviius, M.; Saliba, M.; Lee, Y. H.; Gao, P.; Nazeeruddin, M. K.; Zakeeruddin, S. M.; Rothlisberger, U.; Graetzel, M. Ionic Polarization-Induced Current-Voltage Hysteresis in CH₃NH₃PbX₃ Perovskite Solar Cells. Nat. Commun. 2016, 7 (1), 1–9. https://doi.org/10.1038/ncomms10334.
- (32) Lin, Y.; Bai, Y.; Fang, Y.; Wang, Q.; Deng, Y.; Huang, J. Suppressed Ion Migration in Low-Dimensional Perovskites. *ACS Energy Lett.* **2017**, *2* (7), 1571–1572. https://doi.org/10.1021/acsenergylett.7b00442.
- (33) Cho, J.; Dubose, J. T.; Le, A. N. T.; Kamat, P. V. Suppressed Halide Ion Migration in 2D Lead Halide Perovskites. *ACS Mater. Lett.* **2020**, *2* (6), 565–570. https://doi.org/10.1021/acsmaterialslett.0c00124.
- (34) Zou, Y.; Cui, Y.; Wang, H. Y.; Cai, Q.; Mu, C.; Zhang, J. P. Highly Efficient and Stable 2D-3D Perovskite Solar Cells Fabricated by Interfacial Modification. *Nanotechnology* 2019, 30 (27), 275202. https://doi.org/10.1088/1361-6528/ab10f3.
- (35) Zhang, F.; Kim, D. H.; Zhu, K. 3D/2D Multidimensional Perovskites: Balance of High Performance and Stability for Perovskite Solar Cells. Curr. Opin. Electrochem. 2018, 11,

- 105-113. https://doi.org/10.1016/j.coelec.2018.10.001.
- (36) Quintero-Bermudez, R.; Gold-Parker, A.; Proppe, A. H.; Munir, R.; Yang, Z.; Kelley, S. O.; Amassian, A.; Toney, M. F.; Sargent, E. H. Compositional and Orientational Control in Metal Halide Perovskites of Reduced Dimensionality. *Nat. Mater.* 2018, 17 (10), 900–907. https://doi.org/10.1038/s41563-018-0154-x.
- (37) Koh, T. M.; Shanmugam, V.; Guo, X.; Lim, S. S.; Filonik, O.; Herzig, E. M.; Müller-Buschbaum, P.; Swamy, V.; Chien, S. T.; Mhaisalkar, S. G.; Mathews, N. Enhancing Moisture Tolerance in Efficient Hybrid 3D/2D Perovskite Photovoltaics. *J. Mater. Chem. A* 2018, 6 (5), 2122–2128. https://doi.org/10.1039/c7ta09657g.
- (38) Mitzi, D. B. A Layered Solution Crystal Growth Technique and the Crystal Structure of (C₆H₅C₂H₄NH₃)₂PbCl₄. *J. Solid State Chem.* **1999**, *145* (2), 694–704. https://doi.org/10.1006/jssc.1999.8281.
- (39) Mitzi, D. B.; Chondroudis, K.; Kagan, C. R. Design, Structure, and Optical Properties of Organic–Inorganic Perovskites Containing an Oligothiophene Chromophore. *Inorg. Chem.* **1999**, *38* (26), 6246–6256. https://doi.org/10.1021/ic991048k.
- (40) Kitazawa, N. Compositional Modulation of Two-Dimensional Layered Perovskite (RNH₃)₂Pb(Cl, Br, I)₄ and Its Optical Properties. *Japanese J. Appl. Physics, Part 1 Regul. Pap. Short Notes Rev. Pap.* **1996**, *35* (12 A), 6202–6207. https://doi.org/10.1143/jjap.35.6202.
- (41) Kitazawa, N. Optical Absorption and Photoluminescence Properties of Pb(I, Br)-Based Two-Dimensional Layered Perovskite. *Jpn. J. Appl. Phys.* **1997**, *36* (4 A), 2272–2276. https://doi.org/10.1143/JJAP.36.2272.
- (42) Kitazawa, N.; Yamamoto, T.; Watanabe, Y.; Nakamura, Y. Stability of Self-Assembled Organic-Inorganic Layered Perovskite. In *Materials Research Society Symposium Proceedings*; Materials Research Society, 1999; Vol. 576, pp 165–170. https://doi.org/10.1557/proc-576-165.
- (43) La-Placa, M. G.; Guo, D.; Gil-Escrig, L.; Palazon, F.; Sessolo, M.; Bolink, H. J. Dual-Source Vacuum Deposition of Pure and Mixed Halide 2D Perovskites: Thin Film Characterization and Processing Guidelines. J. Mater. Chem. C 2020, 8 (6), 1902–1908. https://doi.org/10.1039/c9tc06662d.
- (44) Caricato, A. P.; Ge, W.; Stiff-Roberts, A. D. UV- and RIR-MAPLE: Fundamentals and Applications. In Springer Series in Materials Science; Springer Verlag, 2018; Vol. 274, pp 275–308. https://doi.org/10.1007/978-3-319-96845-2_10.
- (45) Stiff-Roberts, A. D.; Ge, W. Organic/Hybrid Thin Films Deposited by Matrix-Assisted Pulsed Laser Evaporation (MAPLE). *Appl. Phys. Rev.* **2017**, *4*, 041303. https://doi.org/10.1063/1.5000509.
- (46) Barraza, E. T.; Dunlap-Shohl, W. A.; Mitzi, D. B.; Stiff-Roberts, A. D. Deposition of Methylammonium Lead Triiodide by Resonant Infrared Matrix-Assisted Pulsed Laser Evaporation. J. Electron. Mater. 2018, 47 (2), 917–926. https://doi.org/10.1007/s11664-017-5814-0.
- (47) Stiff-Roberts, A. D.; Wright, N. E. Two-Dimensional Hybrid Organic-Inorganic Semiconductors Deposited by Resonant Infrared, Matrix-Assisted Pulsed Laser Evaporation. In *Low-Dimensional Materials and Devices 2019*; SPIE, 2019; Vol. 11085. https://doi.org/10.1117/12.2530596.
- (48) Barraza, E. T.; Stiff-Roberts, A. D. Phenomenological Mechanisms of Hybrid Organic-Inorganic Perovskite Thin Film Deposition by RIR-MAPLE. *J. Appl. Phys.* **2020**, *128* (10), 105303. https://doi.org/10.1063/5.0015962.
- (49) Dunlap-Shohl, W. A.; Barraza, E. T.; Barrette, A.; Dovletgeldi, S.; Findik, G.; Dirkes, D. J.; Liu, C.; Jana, M. K.; Blum, V.; You, W.; Gundogdu, K.; Stiff-Roberts, A. D.; Mitzi, D. B. Tunable Internal Quantum Well Alignment in Rationally Designed Oligomer-Based Perovskite Films Deposited by Resonant

- Infrared Matrix-Assisted Pulsed Laser Evaporation. *Mater. Horizons* **2019**, 6 (8), 1707–1716. https://doi.org/10.1039/c9mh00366e.
- (50) Chen, Y.; Yu, S.; Sun, Y.; Liang, Z. Phase Engineering in Quasi-2D Ruddlesden-Popper Perovskites. *J. Phys. Chem. Lett.* **2018**, 9 (10), 2627–2631. https://doi.org/10.1021/acs.jpclett.8b00840.
- (51) Xing, J.; Zhao, Y.; Askerka, M.; Quan, L. N.; Gong, X.; Zhao, W.; Zhao, J.; Tan, H.; Long, G.; Gao, L.; Yang, Z.; Voznyy, O.; Tang, J.; Lu, Z.-H.; Xiong, Q.; Sargent, E. H. Color-Stable Highly Luminescent Sky-Blue Perovskite Light-Emitting Diodes. Nat. Commun. 2018, 9 (1), 3541. https://doi.org/10.1038/s41467-018-05909-8.
- (52) Gao, L.; Zhang, F.; Xiao, C.; Chen, X.; Larson, B. W.; Berry, J. J.; Zhu, K. Improving Charge Transport via Intermediate-Controlled Crystal Growth in 2D Perovskite Solar Cells. Adv. Funct. Mater. 2019, 29 (47), 1901652. https://doi.org/10.1002/adfm.201901652.
- (53) Smith, I. C.; Hoke, E. T.; Solis-Ibarra, D.; McGehee, M. D.; Karunadasa, H. I. A Layered Hybrid Perovskite Solar-Cell Absorber with Enhanced Moisture Stability. Angew. Chemie -Int. Ed. 2014, 53 (42), 11232–11235. https://doi.org/10.1002/anie.201406466.
- (54) Lanty, G.; Jemli, K.; Wei, Y.; Leymarie, J.; Even, J.; Lauret, J. S.; Deleporte, E. Room-Temperature Optical Tunability and Inhomogeneous Broadening in 2D-Layered Organic-Inorganic Perovskite Pseudobinary Alloys. J. Phys. Chem. Lett. 2014, 5 (22), 3958–3963. https://doi.org/10.1021/jz502086e.
- (55) Du, K. Z.; Tu, Q.; Zhang, X.; Han, Q.; Liu, J.; Zauscher, S.; Mitzi, D. B. Two-Dimensional Lead(II) Halide-Based Hybrid Perovskites Templated by Acene Alkylamines: Crystal Structures, Optical Properties, and Piezoelectricity. *Inorg. Chem.* 2017, 56 (15), 9291–9302. https://doi.org/10.1021/acs.inorgchem.7b01094.
- (56) Febriansyah, B.; Koh, T. M.; Lekina, Y.; Jamaludin, N. F.; Bruno, A.; Ganguly, R.; Shen, Z. X.; Mhaisalkar, S. G.; England, J. Improved Photovoltaic Efficiency and Amplified Photocurrent Generation in Mesoporous n = 1 Two-Dimensional Lead-Iodide Perovskite Solar Cells. *Chem. Mater.* 2019, 31 (3), 890–898. https://doi.org/10.1021/acs.chemmater.8b04064.
- (57) Straus, D. B.; Iotov, N.; Gau, M. R.; Zhao, Q.; Carroll, P. J.; Kagan, C. R. Longer Cations Increase Energetic Disorder in Excitonic 2D Hybrid Perovskites. J. Phys. Chem. Lett. 2019, 10 (6), 1198–1205. https://doi.org/10.1021/acs.jpclett.9b00247.
- (58) Shibuya, K.; Koshimizu, M.; Nishikido, F.; Saito, H.; Kishimoto, S. Poly[Bis(Phenethyl-Ammonium) [Di-Bromido-Plumbate(II)]-Di-μ-Bromido]]. *Acta Crystallogr. Sect. E Struct. Reports Online* **2009**, 65 (11), m1323. https://doi.org/10.1107/S160053680903712X.
- (59) Gong, X.; Voznyy, O.; Jain, A.; Liu, W.; Sabatini, R.; Piontkowski, Z.; Walters, G.; Bappi, G.; Nokhrin, S.; Bushuyev, O.; Yuan, M.; Comin, R.; McCamant, D.; Kelley, S. O.; Sargent, E. H. Electron-Phonon Interaction in Efficient Perovskite Blue Emitters. *Nat. Mater.* **2018**, *17* (6), 550–556. https://doi.org/10.1038/s41563-018-0081-x.
- (60) Perdew, J. P.; Burke, K.; Ernzerhof, M. Generalized Gradient Approximation Made Simple. *Phys. Rev. Lett.* 1996, 77 (18), 3865–3868. https://doi.org/10.1103/PhysRevLett.77.3865.
- (61) Tkatchenko, A.; Scheffler, M. Accurate Molecular van Der Waals Interactions from Ground-State Electron Density and Free-Atom Reference Data. *Phys. Rev. Lett.* 2009, 102 (7), 073005. https://doi.org/10.1103/PhysRevLett.102.073005.
- (62) Ren, X.; Rinke, P.; Blum, V.; Wieferink, J.; Tkatchenko, A.; Sanfilippo, A.; Reuter, K.; Scheffler, M. Resolution-of-Identity Approach to Hartree-Fock, Hybrid Density Functionals, RPA,

- MP2 and GW with Numeric Atom-Centered Orbital Basis Functions. *New J. Phys.* **2012**, *14*, 53020. https://doi.org/10.1088/1367-2630/14/5/053020.
- (63) Huhn, W. P.; Blum, V. One-Hundred-Three Compound Band-Structure Benchmark of Post-Self-Consistent Spin-Orbit Coupling Treatments in Density Functional Theory. *Phys. Rev. Mater.* **2017**, *1* (3), 033803. https://doi.org/10.1103/PhysRevMaterials.1.033803.
- (64) Blum, V.; Gehrke, R.; Hanke, F.; Havu, P.; Havu, V.; Ren, X.; Reuter, K.; Scheffler, M. Ab Initio Molecular Simulations with Numeric Atom-Centered Orbitals. *Comput. Phys. Commun.* **2009**, 180 (11), 2175–2196. https://doi.org/10.1016/j.cpc.2009.06.022.
- (65) Havu, V.; Blum, V.; Havu, P.; Scheffler, M. Efficient O (N) Integration for All-Electron Electronic Structure Calculation Using Numeric Basis Functions. J. Comput. Phys. 2009, 228 (22), 8367–8379. https://doi.org/10.1016/j.jcp.2009.08.008.
- (66) Levchenko, S. V; Ren, X.; Wieferink, J.; Johanni, R.; Rinke, P.; Blum, V.; Scheffler, M. Hybrid Functionals for Large Periodic Systems in an All-Electron, Numeric Atom-Centered Basis Framework. *Comput. Phys. Commun.* 2015, 192, 60–69. https://doi.org/10.1016/j.cpc.2015.02.021.
- (67) Williamson, G. K.; Hall, W. H. X-Ray Line Broadening from Filed Aluminium and Wolfram. *Acta Metall.* **1953**, *1* (1), 22–31. https://doi.org/10.1016/0001-6160(53)90006-6.
- (68) Mehrotra, V.; Lombardo, S.; Thompson, M. O.; Giannelis, E. P. Optical and Structural Effects of Aniline Intercalation in PbI2. Phys. Rev. B 1991, 44 (11), 5786–5790. https://doi.org/10.1103/PhysRevB.44.5786.
- (69) Kitazawa, N. Stability of (C₆H₅C₂H₄NH₃)₂Pb(Br_xI_{4-x}) Mixed Crystals. *Jpn. J. Appl. Phys.* **1997**, *36* (Part 1, No. 11), 6876–6879. https://doi.org/10.1143/jjap.36.6876.
- (70) Mosconi, E.; De Angelis, F. Mobile Ions in Organohalide Perovskites: Interplay of Electronic Structure and Dynamics. ACS Energy Lett. 2016, 1 (1), 182–188. https://doi.org/10.1021/acsenergylett.6b00108.
- (71) Boyd, C. C.; Cheacharoen, R.; Leijtens, T.; McGehee, M. D. Understanding Degradation Mechanisms and Improving Stability of Perovskite Photovoltaics. *Chem. Rev.* **2019**, *119* (5), 3418–3451. https://doi.org/10.1021/acs.chemrev.8b00336.
- (72) Brivio, F.; Caetano, C.; Walsh, A. Thermodynamic Origin of Photoinstability in the (CH₃NH₃)Pb(I_{1-x}Br_x)₃ Hybrid Halide Perovskite Alloy. *J. Phys. Chem. Lett.* **2016**, 7 (6), 1083–1087. https://doi.org/10.1021/acs.jpclett.6b00226.
- (73) Barraza, E. T.; Stiff-Roberts, A. D. RIR-MAPLE: Deposition of Hybrid Organic-Inorganic Perovskite Thin Films. In *Hybrid Organic-Inorganic Perovskites: Physical Properties and Applications, vol. 1*; Beard, M. C., Ed.; World Scientific Publishing Co Pte Ltd: Singapore, 2022. (in press)
- (74) Harvey, S. P.; Zhang, F.; Palmstrom, A.; Luther, J. M.; Zhu, K.; Berry, J. J. Mitigating Measurement Artifacts in TOF-SIMS Analysis of Perovskite Solar Cells. *ACS Appl. Mater. Interfaces* **2019**, *11* (34), 30911–30918. https://doi.org/10.1021/acsami.9b09445.
- (75) Harvey, S. P.; Messinger, J.; Zhu, K.; Luther, J. M.; Berry, J. J. Investigating the Effects of Chemical Gradients on Performance and Reliability within Perovskite Solar Cells with TOF-SIMS. Adv. Energy Mater. 2020, 10 (26), 1903674. https://doi.org/10.1002/aenm.201903674.
- (76) Heyd, J.; Scuseria, G. E.; Ernzerhof, M. Hybrid Functionals Based on a Screened Coulomb Potential. *J. Chem. Phys.* 2003, 118 (18), 8207–8215. https://doi.org/10.1063/1.1564060.
- (77) Heyd, J.; Scuseria, G. E.; Ernzerhof, M. Erratum: Hybrid Functionals Based on a Screened Coulomb Potential (Journal of Chemical Physics (2003) 118 (8207)). *J. Chem. Phys.* **2006**, 124 (21), 219906. https://doi.org/10.1063/1.2204597.

- (78) Liu, C.; Huhn, W.; Du, K. Z.; Vazquez-Mayagoitia, A.; Dirkes, D.; You, W.; Kanai, Y.; Mitzi, D. B.; Blum, V. Tunable Semiconductors: Control over Carrier States and Excitations in Layered Hybrid Organic-Inorganic Perovskites. *Phys. Rev. Lett.* 2018, 121 (14), 146401. https://doi.org/10.1103/PhysRevLett.121.146401.
- (79) Jana, M. K.; Song, R.; Liu, H.; Khanal, D. R.; Janke, S. M.; Zhao, R.; Liu, C.; Valy Vardeny, Z.; Blum, V.; Mitzi, D. B. Organic-to-Inorganic Structural Chirality Transfer in a 2D Hybrid Perovskite and Impact on Rashba-Dresselhaus Spin-Orbit Coupling. *Nat. Commun.* 2020, 11 (1), 4699. https://doi.org/10.1038/s41467-020-18485-7.
- (80) Jana, M. K.; Janke, S. M.; Dirkes, D. J.; Dovletgeldi, S.; Liu, C.; Qin, X.; Gundogdu, K.; You, W.; Blum, V.; Mitzi, D. B. Direct-Bandgap 2D Silver-Bismuth Iodide Double Perovskite: The Structure-Directing Influence of an Oligothiophene Spacer Cation. J. Am. Chem. Soc. 2019, 141 (19), 7955–7964. https://doi.org/10.1021/jacs.9b02909.
- [81] Jana, M. K.; Liu, C.; Lidin, S.; Dirkes, D. J.; You, W.; Blum, V.; Mitzi, D. B. Resolving Rotational Stacking Disorder and Electronic Level Alignment in a 2d Oligothiophene-Based Lead Iodide Perovskite. *Chem. Mater.* 2019, 31 (20), 8523– 8532. https://doi.org/10.1021/acs.chemmater.9b03208.
- (82) Gao, Y.; Shi, E.; Deng, S.; Shiring, S. B.; Snaider, J. M.; Liang, C.; Yuan, B.; Song, R.; Janke, S. M.; Liebman-Peláez, A.; Yoo, P.; Zeller, M.; Boudouris, B. W.; Liao, P.; Zhu, C.; Blum, V.; Yu, Y.; Savoie, B. M.; Huang, L.; Dou, L. Molecular Engineering of Organic-Inorganic Hybrid Perovskites Quantum Wells. *Nat. Chem.* **2019**, *11* (12), 1151–1157. https://doi.org/10.1038/s41557-019-0354-2.



